International Space Planes and Hypersonic Systems and Technologies Conferences
6-9 March 2017, Xiamen, China
21st AIAA International Space Planes and Hypersonics Technologies Conference

10.2514/6.2017-2444

A low-dissipation solver based on OpenFOAM designed for large eddy simulation in compressible flows

Yachao Lee[1], Wei Yao[2] and Xuejun Fan[3]

a. *State Key Laboratory of High Temperature Gas Dynamics, Institute of Mechanics, CAS, Beijing 100190, China*

b. *School of Engineering Science, University of Chinese Academy of Sciences, Beijing 100049, China*

To reduce the numerical dissipation in compressible flow modeling, a low-dissipation compressible solver is developed for large eddy simulation based on the original compressible solver rhoCentralFoam within the framework of an open source computational fluid dynamics package OpenFOAM. In rhoCentralFoam, the central-upwind scheme of Kurganov and Tadmor is applied to capture flow discontinuities, but its dissipation is too strong to resolve fine turbulence structures under finite mesh resolutions. The current low-dissipation solver adopts a new hybrid scheme, which combines the dissipative Kurganov-Tadmor scheme with the nondissipative central scheme. By aid of a shock sensor, the dissipative scheme is used to capture the flow discontinuities near shock waves and the central scheme is used to resolve the turbulence structures in the smooth flow area. In the framework of unstructured mesh, the central scheme is extended from second order to forth order, which greatly reduces the dispersion error and weakens the oscillations near flow discontinuities. To improve the numerical stability of the central scheme, the skew-symmetric form of the convective term is adopted to preserve the local kinetic energy and maintain the self-stability of central scheme without adding an explicit dissipative term. In addition, a low-storage third-order TVD Runge-Kutta method for temporal discretization is newly implemented in the low-dissipation solver to further reduce the numerical dissipation. A series of benchmark flow problems, such as Sod shock tube test, Shu-Osher problem, Green-Taylor vortex evolution, and wall-bounded turbulence generation based on synthetic eddy method, are computed and compared to examine the low-dissipation solver's capability in capturing flow discontinuities as well as resolving fine turbulence structures. The accuracy and stability of the low-dissipation solver are further validated against experimental data for a scramjet model with a supersonic airstream passing over the flame holder structure.

Nomenclature

U = velocity vector
F = interface flux
γ = specific heat ratio
ρ = density
Q = the second invariant of velocity gradient
δ = boundary layer thickness
θ = momentum thickness
Θ = shock sensor
E = total energy
c = sound speed
p = pressure

---

[1] PhD candidate, Institute of Mechanics(CAS), liyachao@imech.ac.cn, AIAA member.
[2] Associate Professor, Institute of Mechanics(CAS), weiyao@imech.ac.cn, AIAA member, corresponding author.
[3] Professor, Institute of Mechanics(CAS), xfan@imech.ac.cn, AIAA lifetime member, corresponding author.

T = temperature
V = volume
l = length
L = differential operator
c_f = wall friction coefficient
u_τ = friction velocity
κ = wave number/ Karman constant
Ω = total enstrophy
D = cavity depth
ω = specific turbulent dissipation rate or velocity vorticity
k = turbulent kinetic energy
u,v,w = components of velocity vector
x,y,z = Cartesian coordinates
i,j = computational indices

Superscripts

n	denotes the time level in the time marching method
$+$	denotes variables normalized by wall friction properties
$*$	denotes variables normalized by the characteristic scale of the flowfield or the distance along the wall surface
$'$	denotes fluctuations

Subscripts

w	denotes a flow property at the wall
∞	denotes the farfield conditions
0	denotes the initial conditions
vd	denotes von Driest transformation

I. Introduction

THE severely complex indoor flow environment of scramjet combustion poses a huge challenge to computational fluid dynamics (CFD), due to the complex, nonlinear interactions between viscous wall-bounded flows, mixing layers, shocks, thermodynamic and chemical nonequilibrium flow physics brought by combustion. For many years, the Reynolds-averaged Navier-Stokes (RANS) modeling approach has been the routine when the effects of turbulence are considered, which models the turbulence motion at all scales as well its effects on other processes, such as the mixing of species, momentum, and energy. However, in the scramjet the interaction between turbulence and chemical kinetics plays a leading role, which makes this flow regime extremely difficult to model, because no assumptions can be accurately postulated about the relationships between temporal and spatial scales of multiple phenomena. Therefore, these dynamic interactions of multiphysics and multiscales must be simulated rather than modeled. The large eddy simulation (LES) approach only requires modeling the universal small-scale structures, whereas the large-scale structures are resolved naturally through the solution of the filtered governing equations. Since the most challenging dynamic interactions, including the mass, momentum and energy transfer, occur in the large scales, the LES approach actually reduces the difficulty of modeling all kinds of flow phenomenon. Compared with RANS method, LES puts forward higher requirements on the numerical methods used to discretize and advance the Navier-Stokes equations. In particular, LES requires high temporal accuracy, and minimal intrinsic numerical dissipation and dispersion over a wide range of length scales. In addition, the stability and reliability of the numerical methods need serious considerations.

Kurganov-Tadmor scheme[1] is employed in a density-based solver rhoCentralFoam in OpenFOAM, which is aimed at solving compressible flow problems with strong flow discontinuities. The scheme is a new central-upwind scheme after Lax-Friedrichs scheme[2] and Nessyahu-Tadmor scheme[3], which belongs to the Riemann-solver-free approach. The main idea behind Kurganov-Tadmor scheme is the use of more precise information of the local propagation speeds and realization of the nonsmooth part of the approximate solution in terms of its cell averages integrated over the Riemann fans of varying size. Though it bears a much smaller numerical viscosity than its counterpart does, Kurganov-Tadmor scheme is still a shock-capturing method, which will produce excessive numerical dissipation in the whole flow field in order to capture the discontinuity. However, the excessive numerical dissipation will submerge the physical viscosity of the flowfield itself, especially in the smooth flow regions, causing the simulation with LES method close to the results using RANS.

Central difference scheme is an ideal candidate for computations free of spurious numerical diffusivity, due to its none-dissipation error in a linear setting. Central derivative scheme has been widely used before, especially for wave propagation problems[4] in which nonlinearities are weak. However, because of the accumulation of the aliasing errors resulting from discrete evaluation of the nonlinear convective terms, standard central discretization of fluid turbulence in high Reynolds number flow typically will lead to numerical instability. Though finite physical viscosity may help to stabilize the calculation, it is usually safer to revert to alternative discretization techniques to ensure stability in the inviscid limit. Most efforts are based on the idea of splitting the convective terms in skew-symmetric form, which implies kinetic energy preservation at the semi-discrete level[5]. However, if discontinuities are present, the scheme is not as robust and artificial dissipation must be added in the vicinity of the discontinuities or the scheme must be hybridized with a scheme capable of capturing the discontinuities. In this paper, the hybridization methods are used to formulate the low-dissipation solver.

A key ingredient in the formulation of hybrid schemes is the proper specification of the shock sensor[6], which must be defined that numerical dissipation is effectively confined around shocked regions, so that it does not pollute smooth parts of the flowfield. Adams[7] and Pirozzoli[8] have used a sensor formulation based solely on the local flow gradients. Hill[9] and Pantano[10] used the Jameson-type sensor based on both pressure and density fields in their hybrid scheme. Ducros[11] introduced a simple sensor based on the physical observation that the turbulent structures are essentially vertical, whereas the shock waves are usually associated with the bulk dilatation of the flow, which was frequently referred to as the Ducros sensor. A more elaborate sensor for shock waves and shears based on the multiresolution wavelet analysis were proposed by Yee[12].

The purpose of this paper is to constitute a low-dissipation compressible solver within the OpenFOAM framework to deal with the complex flowfields in the scramjet with unsteady flow phenomenon as well as strong shock waves in the high Reynolds number. A hybridization formulation of the convective operator derived from the central scheme in skew-symmetric form and Kurganov-Tadmor scheme is put forward to resolve the small-scale turbulence structures in smooth flow regions as well as to capture the flow discontinuities in the presence of shock waves. In addition, a low-storage TVD (total variations diminishing) Runge-Kutta method for third order temporal discretization and a hybrid RANS/LES method are newly implemented in the new solver to make the time marching and deal with wall-bounded flow, respectively. A serious of benchmark problems with increasing spatial and fluid dynamic complexity, such as Sod shock tube test, Shu-Osher problem, Green-Taylor vortex evolution problem and wall-bounded turbulent flow, will be employed to examine the ability of the low-dissipation solver in dealing with various flow conditions. Finally, an extensive investigation with these validated methods is conducted to simulate the complex flowfield as supersonic airstream flows past the typical flame holder structure in the scramjet model.

II. Numerical methods

The high-speed flows with strong shock waves bring a huge challenge to the numerical methods using LES method. On the one hand, a scheme of high resolution and tiny numerical dissipation is required in the smooth regions to resolve the fine turbulence structures. On the other hand, in the flowfields with strong shock waves, the diffusive scheme is necessary to help maintain the stability of the simulation and avoid the Gibbs oscillation around the flow discontinuities. Neither the classical shock-capturing methods, such as TVD or Godunov scheme, nor the spectral-like scheme could meet such requirements simultaneously. Therefore, hybridization formulation of the convective operator is a natural choice, where the diffusive scheme takes effect in shocked regions whereas the nondissipative scheme is utilized elsewhere.

The general formulation of a hybrid low-dissipation scheme in the finite volume framework is achieved through the hybridization of the inviscid interface flux, which corresponds to the convective term in the Navier-Stokes equations. This step is usually accomplished by the linear combination of a central nondissipative flux and a conventional dissipative flux as follows

$$F_{hybrid} = \Theta F_{dissipative} + (1-\Theta) F_{centeral} \tag{1}$$

where F is the interface flux and Θ is the shock sensor. The dissipative flux $F_{dissipative}$ is calculated from Kurganov-Tadmor scheme, where the primitive variables are derived from Monotonic Upstream-Centered Scheme for Conservation Laws (MUSCL) reconstruction method with low-dissipation limiters, such as SuperBee or vanLeer. The nondissipative flux is constructed from the central scheme in skew-symmetric form. In this paper, the central scheme in skew-symmetric form of Kennedy and Gruber[13] is adopted, which is reproduced as below

$$F_{central} = \frac{\rho_i + \rho_j}{2} \frac{u_i + u_j}{2} \frac{\varphi_i + \varphi_j}{2} \tag{2}$$

where φ stands for a genetic transport scalar, such as velocity component or internal energy. The Eq.(2) represents a robust convective formulation, which minimizes both aliasing error and computational cost. On uniform curvilinear grids, every primitive variables need linearly interpolating before formulating the interface flux.

Another critical aspect is concerned with the dispersive properties of the scheme, which are of great importance in simulating unsteady flow. The numerical dispersion errors can be reduced by using appropriate central finite difference schemes, such as the dispersion-relation preserving (DRP) scheme of Tam and Webb[14], and the compact scheme of Lee[15]. Kok[16] used the DRP approach to minimize the dispersion by using a lager stencil in the Richardson extrapolation on nonuniform, curvilinear, structured grids within the finite volume method. However, these techniques are hard to be generalized to the unstructured solver duo to the exchange of grid information addressing methods in structured grids. Therefore, linear scheme, as the second order central scheme, is commonly used in unstructured solver, which only needs the cell-center value of adjacent cells. Even so, the gradient information of adjacent cells can also be employed to improve the dispersion properties of the central scheme in unstructured grids. Inspired by this, the forth order central scheme is constructed to reconstruct the values at interface based on the information of the cell-center value and gradients of adjacent cells. The formulation of a forth order scheme in unstructured grids on uniform Cartesian grids is as follows

$$\phi_f = \frac{1}{2}(\phi_i + \phi_j) + \frac{1}{3}(\nabla\phi_i - \nabla\phi_j)\cdot d_{ij} \tag{3}$$

where ϕ represents the primitive variables p, ρ, and U. d_{ij} is the displacement vector between the centers of two adjacent cells. Similar treatment is also found in the research of Peterson[17], Khalighi[18], and Lowe[19]. The improved central scheme could effectively minimize the numerical dispersion errors in the calculations.

In the hybridization formulation, the shock sensor is used as a switch, which dynamically adjusts the solver for conditions near to and away from flow discontinuities. As mentioned before, the Ducros sensor represents a simple and frequently adopted choice, which has the form

$$\Theta = \frac{(\nabla\cdot U)^2}{(\nabla\cdot U)^2 + (\nabla\times U)^2 + \varepsilon} \tag{4}$$

where ε is a small number to prevent division by zero. It is only activated when the local dilatation becomes larger than a typical large-scale velocity gradient. Previous investigations for the direct numerical simulation of transonic shock/boundary layer interactions[20] suggest that the Ducros sensor is capable of selectively isolating genuine shocks, whereas other shock sensors, such as Jameson sensor[21], Hill&Pullin sensor[22] and Visbal&Gaitonde sensor[23], also mark smooth regions populated by vortex structures as critical zones.

However, in a detailed research by Kawai[24] for decaying compressible isotropic turbulence with eddy shocklets, the Ducros sensor is found unable to distinguish shocks from regions of expansion and weakly compressible turbulence regions without shocks, thus it is will lead to the damp of the evolution of density and dilatation in these continuous flow areas. The negative dilatation sensor combined with Ducros sensor is introduced in the paper to avoid such deficiency. Taking these into consideration, a modified formulation of Ducros sensor by Bhagatwala[25] is put forward, which has the form

$$\Theta = \frac{1}{2}\left(1 - \tanh\left(2.5 + 10\frac{\Delta}{c}\nabla\cdot U\right)\right) \times \frac{(\nabla\cdot U)^2}{(\nabla\cdot U)^2 + (\nabla\times U)^2 + \varepsilon} \tag{5}$$

where c is the local speed of sound, and Δ is the cell length scale. The factor 10Δ/c in front of the dilatation is a scaling term, which makes the grid dependent numerical dilatation invariant to mesh size and also appropriately normalizes the dilatation.

The main difference of the modified formulation from Ducros sensor is that it turns the dissipative scheme on or off based on the magnitude and sign of dilatation. In particular, the shock sensor approaches to zero for positive dilatation where the expansion wave occurs, and it rises slowly as the negative dilatation increases in magnitude. Only if the time period of the acoustic wave is less than 1/10th of the temporal scale of the dilatation, does the dissipative scheme start taking effect. Near the strong flow discontinuities, the shock sensor gets close to unity. Since shock waves are a region of high negative dilatation, the new formulation makes shock-capturing method only activated in such areas. For the sake of numerical stability, the shock sensor in this paper is bounded by 0.1 and 1.0, unless otherwise specified.

To make the time marching, a low-storage TVD Runge-Kutta method for third order temporal discretization by Gottlieb and Shu[26] is implemented. Compared with the non-TVD but linearly stable Runge-Kutta method, the optimal TVD Runge-Kutta for third order is more suitable to solve the hyperbolic problems, which has the form

$$\begin{cases} u^{(1)} = u^n + \Delta t L(u^n) \\ u^{(2)} = \frac{3}{4}u^n + \frac{1}{4}u^{(1)} + \frac{1}{4}\Delta t L(u^{(1)}) \\ u^{n+1} = \frac{1}{3}u^n + \frac{2}{3}u^{(2)} + \frac{2}{3}\Delta t L(u^{(2)}) \end{cases} \tag{6}$$

where u represents the three conservative variables ρ, ρU and ρE, Δt is the time-step size, superscript n represents the time level, superscript (1) indicates the iteration level in every time-step, L(u) is the spatial derivatives of these variables.

A hybrid RANS/LES method[27,28] based on the k-ω SST model is implemented to the low-dissipation solver to model the effect of subgrid scales. It is an improved delayed detached eddy simulation (IDDES), which combines detached eddy simulation (DES) and wall modeled large eddy simulation (WMLES) according to the inflow turbulence content. The IDDES method allows RANS to model the small-scale turbulence in near wall region in order to relive the huge grid requirements, and LES to resolve the large-scale turbulence away from the wall.

In the following section, the low-dissipation solver, which adopts the hybrid scheme and 3rd TVD Runge-Kutta temporal discretization method, is named hybridCentralFoam. Another solver follows the same formulation, but its shock sensor is set to a constant value 1.0 to produce shock-capturing scheme everywhere. The dissipative solver is named rhoCentralFoam to manifest that it enjoys the equivalent numerical scheme with the original solver in OpenFOAM.

III. Discontinuous Problems

The capture of physical discontinuity is essential for the numerical simulations of supersonic turbulent flows. A series of test cases for shock-capturing schemes have been proposed in the literature. These tests have been designed to assess the capacity of different numerical schemes in resolving fundamental features of supersonic flows, as well as some particularly challenging configurations. Since the numerical characteristics of Kurganov-Tadmor scheme has been verified in Ref.29, the following section will outline the low-dissipation solver's ability in capturing discontinuity as well as stability and fidelity in complex supersonic flow conditions.

A. Sod shock tube

The Sod shock tube problem[30] is a common test case to examine the behavior of the dissipative discontinuity-capturing advection schemes. The time evolution of this problem can be described by solving the inviscid Euler equations, which leads to three characteristics, namely the rarefaction wave, the contact discontinuity and the shock discontinuity. The numerical results can be validated against the analytical solution in order to assess how well the schemes capture the shock waves and contact discontinuities, reproduce the density profile of the rarefaction wave.

The initial flow variables distribution follows the shock tube experiment, where the flow field is subdivided into two blocks by an immediate diaphragm. The computational domain is discretized with 100 cells with uniform spacing from x=-5 to x=5. The left boundary is treated as a supersonic inflow where all the primitive variables are specified with a fixed value as follows, and the right boundary is an outflow in which all the variables are determined from the internal filed. The gas obeys a calorically perfect gas equation of state with the specific heat ratio of γ=1.4 (the same as below).

$$(\rho, u, p) = \begin{cases} (1,\ 0,\ 10),\ x \le 0 \\ (0.125,\ 0,\ 1),\ x > 0 \end{cases} \tag{7}$$

The flow field begins to evolve from the initial conditions at t=0, just as the diaphragm instantaneously burst. The initial interface soon forms a right-moving shock, a left-moving rarefaction fan and an intermediate contact discontinuity. Fig.1 demonstrates the computed (using hybridCentralFoam) and the analytic density and pressure profiles at a nondimensional time of *t*=0.007, which could reveal the key physical phenomenon of the shock tube flow. With the current method, all waves are correctly captured at their right propagation speed. Futhermore, the contact discontinuity are smeared over a few cells, but their behavior is otherwise well simulated. Overall, this shock-capturing method is well adapted to the capture of discontinuities in supersonic flows.

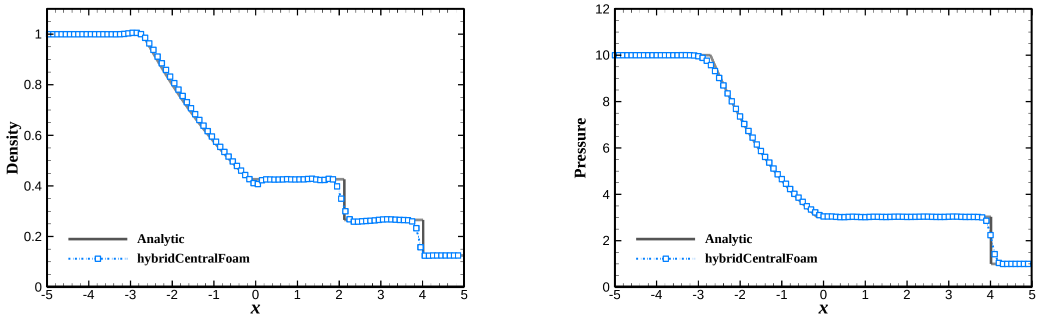

a) density distribution **b) pressure distribution**

Figure 1. Density and pressure profiles for Sod shock tube problem

B. Shu-Osher test case

This is a one-dimensional idealization of shock-turbulence interaction, in which a shock propagates into a perturbed sinusoidal density field[31]. As the shock passes through, it is immediately followed by a region of rapid, high amplitude oscillations. These short wavelengths oscillations decay further downstream of the shock, forming a region of longer wavelength oscillations, which steepen into shocks, forming an N-wave pattern. A complete capture of the entire phenomenon and all wavelengths requires a fairly high resolution. This makes this simple test case particularly relevant to the problem of shock/turbulence interaction. The initial conditions for this problem are given as follows:

$$(\rho,u,p)=\begin{cases}(3.857143,\ \ 2.629369,\ \ 10.33333), & x<-4\\ (1+0.2\sin(5x),\ \ \ 0,\ \ \ 1), & x\geq -4\end{cases} \tag{8}$$

The domain is $x\in[-5,5]$ with the uniform grid spacing $\Delta x=10/200$. The simulation is finalized at a time of t=1.8. As the velocity and pressure profiles do not contain as much interesting flow structures, only the results for the density distribution are compared in Fig.2. The reference solution[32] was obtained on a very fine mesh (1800 points) using the fifth-order WENO scheme.

In Fig.2, it’s easy to see that the dissipative solver rhoCentralFoam cannot capture the short-wavelength oscillations after the shock wave. In this region, the dominant wavenumber of the N-wave pattern appears as the smallest resolved wavenumber. In contrast, the low-dissipation method hybridCentralFoam leads to a crisp capture of the shock front using the dissipative scheme, whereas the smooth nondissipative scheme is used to resolve the post-shock region. As a consequence, despite the fact that the full amplitude of the oscillations is not totally recovered, most of the short wavelengths are obtained in the post-shock region at such low-resolution simulation. Overall, the hybrid approach hybridCentralFoam combines the advantages of both schemes, leading to a proper capture of the main shock and a very good resolution of the post-shock oscillations.

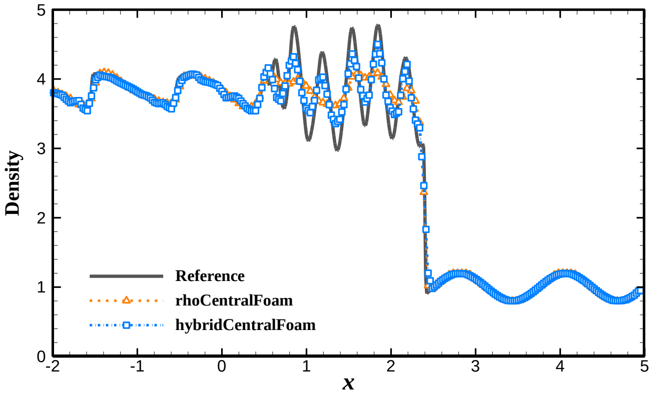

Figure 2. Density profiles for Shu-Osher problem (200 points)

C. Supersonic flow over forward-facing step

The problem represents a 2D inviscid supersonic flow problem with discontinuous phenomenon, which was originally proposed by Emery[33] to examine the performance of shock-capturing schemes. In particular, we consider the flow configuration used by Woodward and Colella[34], where the supersonic flow at Mach 3 to a rectangular channel with a step near the inlet region. The geometric sketch of the forward-facing step is briefly shown in Fig.3. Slip boundary conditions are imposed at the top and lower walls, and all variables are extrapolated at the outlet and normalized.

Instantaneous temperature contours at time t=3 for rhoCentralFoam and hybridCentralFoam are illustrated in Fig.4. Inspection of the shock pattern shows that, in spite of some qualitative similarities, hybridCentralFoam delivers additional flow details, which are barely visible with rhoCentralFoam. In particular, the spanwise vortex due to entropy gradient issuing from the quadruple point near the top wall is distinct in Fig.4b), but obscure in Fig.4a). The higher numerical dissipation of the rhoCentralFoam solver is responsible for the results. Quantitative differences are also found in the prediction of the Mach stem at the step wall, which is much taller in Fig.4a). Fig.5 shows contours of the shock sensor corresponding to the field shown in Fig.4b), which highlights the regions in which the convective diffusive flux is activated. This is a convincing confirmation that numerical dissipation is only activated in close vicinity of shock wave.

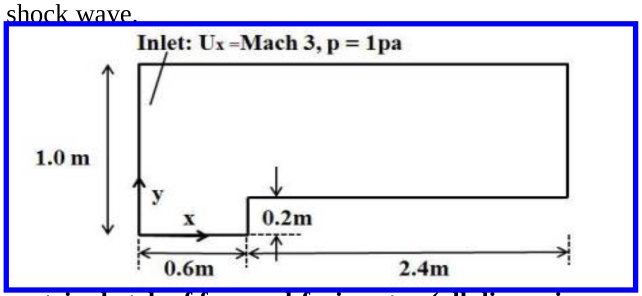

Figure 3. Geometric sketch of forward-facing step (all dimensions are normalized)

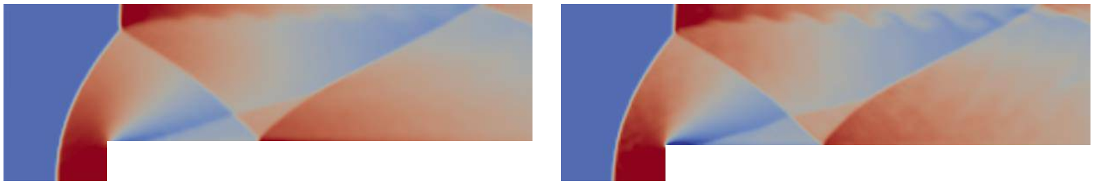

a) rhoCentralFoam **b) hybridCentralFoam**

Figure 4. Temperature contours of the supersonic flow over forward-facing step at Ma_∞=3

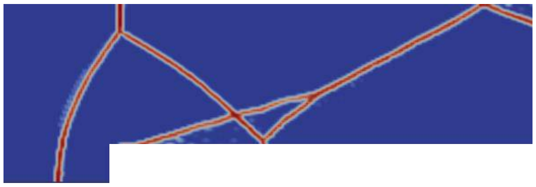

Figure 5. Contours of the shock sensor of the supersonic flow over forward-facing step using hybridCentralFoam

IV. Continuous Problems

In addition to precisely capture the flow discontinuity, the low-dissipation solver should be able to resolve the turbulence structure in smooth flow region, which is critical to the fuel mixing and turbulent combustion process in the indoor flow environment simulation of scramjet. For this reason, the following section will focus on testing and verifying the low-dissipation solver's performance in the turbulence evolution in both inviscid and viscous Taylor-Green vortex problem as well as the wall-bounded compressible turbulent flow.

A. Taylor-Green vortex problem

The test case is typically set to assess the numerical discretization schemes for scale-resolving simulation approaches. Here both the inviscid and viscous Taylor-Green vortex problems are investigated. In the inviscid flow, the initial large-scale vortex will continually evolve to smaller structures as the process found in turbulent flow. However, there is no lower bound on the length scale of these structures because the dissipation provided by the convective scheme is the unique source in this case. Therefore, the inviscid Taylor-Green vortex problem by Johnsen[35] is used to examine the stability of the smooth flow, nondissipative scheme for severely under-resolved scales and to test their ability of temporally conserving the total kinetic energy. On the other hand, in the viscous Taylor-Green problem, starting from an analytical periodic 3D vortex field, the large coherent structure begin to interact and develop smaller and smaller vortices, which finally break up into fine scale decaying homogeneous turbulence.

The solution is computed on a periodic cube domain, $-\pi l \leq x, y, z \leq \pi l$. The flowfield is initialized with

$$\begin{aligned}
u &= U_0 \sin(\frac{x}{l}) \cos(\frac{y}{l}) \cos(\frac{z}{l}) \\
v &= -U_0 \cos(\frac{x}{l}) \sin(\frac{y}{l}) \cos(\frac{z}{l}) \\
w &= 0 \\
p &= p_0 + \frac{\rho_0 U_0^2}{16} [\cos(\frac{2x}{l}) + \cos(\frac{2y}{l})][\cos(\frac{2z}{l}) + 2]
\end{aligned} \tag{9}$$

where l=0.01m, p_0=7271Pa, T_0=298.15K, and U_0=34.6115m/s. The flow is effectively incompressible, which corresponds to Mach number of Ma=0.1. The initial condition for density ρ_0 is calculated by the perfect gas law, where fixed temperature is assumed. Calculations are performed on three grid sizes: 64×64×64, 128×128×128 and 256×256×256, with uniform grid spacing throughout the domain. Periodic boundary conditions are applied to all directions. The computation time t is normalized by a characteristic time scale of the problem, that is $t^*=t/(l/U_0)$. All the calculations are run to 20 characteristic time scale and the maximum Courant-Friedrichs-Lewy (CFL) number is no more than 0.3. Here the threshold value of the shock sensor in the inviscid case is set to 0.

Firstly, numerical investigations are conducted to examine the stability of the smooth flow by nondissipative scheme when the viscous terms are removed from the Navier-Stokes equations. The temporal evolution of the total kinetic energy for the computational domain is illustrated in Fig.6. Here E_k represents the normalized kinetic energy and is given by

$$E_k = \frac{1}{\rho_0 V U_0^2} \int_\Omega \rho U^2 / 2dV \tag{10}$$

where V is the volume of computational domain. The results show that the low-dissipation solver could preserve the kinetic energy with only a small decrease at the end of the simulation. It should be mentioned that the total kinetic energy with the dissipative solver diverges shortly after the computation starts. Overall, these inviscid simulations confirm the kinetic energy conservation property of the skew-symmetric scheme.

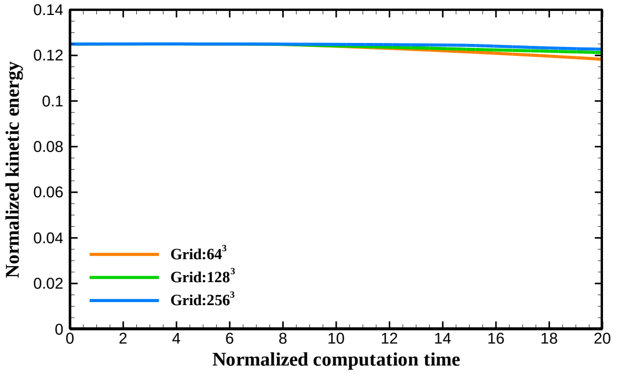

Figure 6. Temporal evolution of total kinetic energy for the inviscid Taylor-Green vortex

Secondly, the viscous Taylor-Green vortex problem is considered. This is a benchmark case, which simulates the flow field from a smooth initial condition to fully developed turbulence after a series of vortex stretching and transition. The case is solved with the Reynolds number based on the reference length l and velocity U_0 of Re=1600. No turbulence model is applied and the results will be compared with the spectral DNS simulation[36,37].

The temporal evolution of Taylor-Green vortex flowfield can be visualized by showing its iso-surface of Q-criterion as depicted in Fig.7. The iso-surfaces are colored with the normalized velocity magnitude $U^*=|U|/U_0$. At the earliest time the initial large-scale vortex structure begins to evolve and role up. Nearly t^*=6.9, the smooth vertical structures begin to undergo change and around t^*=9.0, the coherent structures breakdown and transition to turbulence. Beyond this, the flow is fully turbulent and proceeds steadily to a decaying isotropic state until the flow comes to rest. It is also evident that the reduction in overall kinetic energy is visible with the velocity magnitude color scales as the simulations progress.

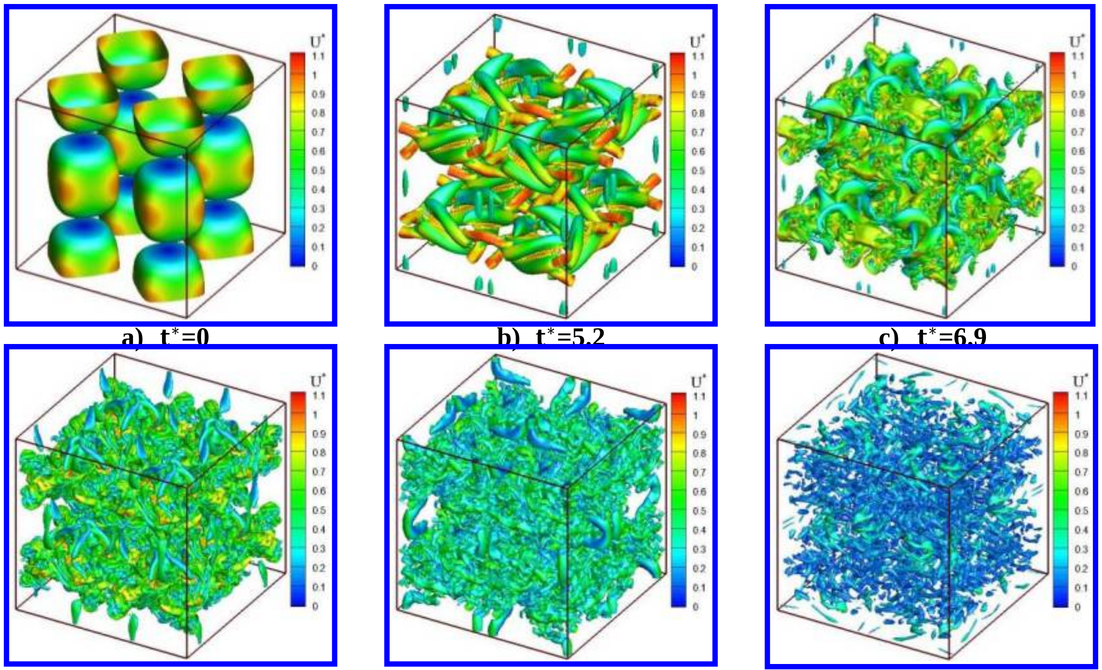

a) $t^*=0$ b) $t^*=5.2$ c) $t^*=6.9$

d) $t^*=9.0$ e) $t^*=12.1$ f) $t^*=20$

Figure 7. Temporal evolution of the Taylor-Green vortex at Re=1600 visualized by iso-surface of Q-criterion with mapped-on normalized velocity magnitude

The history of total kinetic energy E_k for the viscous cases at Re=1600 are illustrated in Fig.8. The results are in good agreement with the reference DNS data, though slight departure exists at the poorest resolution. To further validate the performance of the skew-symmetric form in turbulence energy transfer, the temporal development of the dissipation rate of total kinetic energy for the computational domain is considered, which is defined as $\varepsilon=-\partial E_k/\partial t$. This value is calculated from the total kinetic energy using standard second order central differences for all points except for the first and last time history points (which use one-sided differences). Another critical parameter measuring the dissipation rate is the total enstrophy in the flow domain, which is given by

$$\Omega = \frac{l^2}{\rho_0 V U_0^2}\int_{\Omega} \rho\omega\cdot\omega / 2dV \qquad (11)$$

where ω is the vorticity vector. The temporal evolution of ε and Ω on three grid sets are compared with high-resolution spectral DNS data, which are presented in Fig.9 and Fig.10, respectively. The enstrophy-based dissipation rate Ω drastically underpredicts the actual dissipation rates and shows a large grid dependency. This can be explained by the use of the vorticity in Eq.(11), which are computed using standard Green-Gauss gradients. The dissipation rate ϵ directly derived from the kinetic energy gives much more accurate results for all three resolutions. On the finest grid, ϵ follows the DNS data closely up to $t^*\approx 8$, but fails to predict the peak value at $t^*\approx 9$. On the coarser grids, the deviation from the reference results starts even earlier. The investigations made for viscous Taylor-Green vortex are considered as a strong indication that the low-dissipation solver are beneficial in correctly predicting such a complex flow development with an energy cascade from large to small scales.

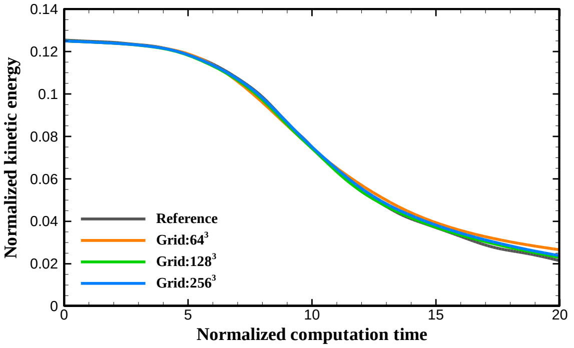

Figure 8. Temporal evolution of total kinetic energy for the viscous Taylor-Green vortex at Re=1600

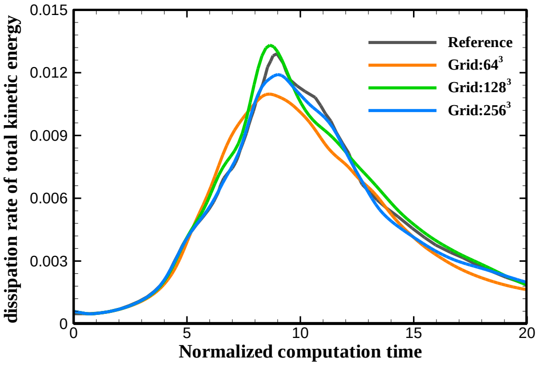

Figure 9. Temporal evolution of the dissipation rate of total kinetic energy for the viscous Taylor-Green vortex

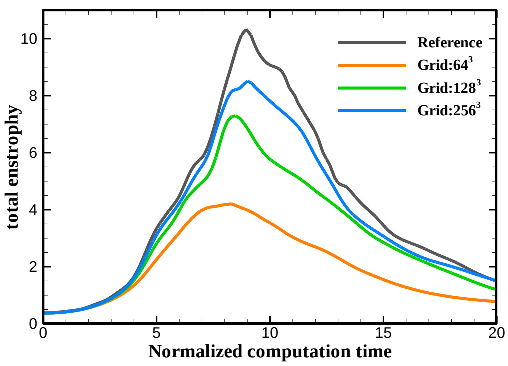

Figure 10. Temporal evolution of the total enstrophy for the viscous Taylor-Green vortex

B. Fully developed turbulent flow

This problem is used to assess the capability of the low-dissipation solver approach on the wall-bounded compressible turbulent flow. Within the boundary layer, huge velocity vorticities will make the Ducros-type sensor diminish to the threshold value and the central scheme will dominant in the solution. Therefore, such case is set to examine the performance of the low-dissipation solver in resolving fine turbulence structures under the certain grid resolution, as well as its capacity of dealing with compressible wall-bounded flow using current LES methods. In this case, the supersonic flat plate flow at a freestream Mach number of Ma$_{\theta}$=2 with the Reynolds number based on the momentum thickness of Re$_{\theta}$=2000 is investigated. Furthermore, the IDDES method based on Menter's k-ω SST model is applied to deal with the turbulence structure of multiple scales.

A reformulated synthetic turbulence generation method by Roidl[38] is employed to generate a time-varying inflow boundary conditions. The method is based on the work of Jarrin[39] and Pamies[40], which describes turbulence as a superposition of coherent structures. Compared to the former, the novel formulation uses the momentum thickness Reynolds number not the boundary layer thickness to describe the spatial and temporal characteristics of the turbulence structure, and takes the normal motion of virtual vortex into account. It does not require additional control planes to yield a short transition length, and has been transformed to be applicable to both subsonic and supersonic flows. Furthermore, the velocity fluctuations statistics and Reynolds stress tensor, which are necessary for the synthetic turbulence method, are extracted from a DNS solution for a flat-plate boundary-layer configuration of Spalart[41] at Re_{θ}=1440. Strong Reynolds analogy at the inflow boundary is enforced to relate the temperature fluctuation and the velocity fluctuations, which have been obtained through the synthetic turbulence method.

Meanwhile, the inflow boundary conditions for the mean velocity and temperature profiles are introduced as follows. For the moderate compressible flows, Morkovin's hypothesis asserts that compressibility or Mach number only affects the turbulence (as well as velocity correlations) through variants in mean density, and that the fluctuation in density ρ' has little effect on the turbulence. The von Driest transformation is used to correlate the mean velocity profile in compressible flow with the incompressible case, where the composite velocity laws in incompressible are employed. In the meantime, the corrected Crocco's correlation between temperature and velocity profiles for the zero-pressure-gradient flat plane is applied to obtain the inflow mean temperature profiles.

The computational domain size for the LES application is 24δ, 2.5δ, and 5δ in streamwise, spanwise, and wall-normal directions. A uniform grid spacing, dx^+= 25 and dz^+= 10, is used in streamwise and spanwise directions up to x=20δ. In the wall-normal direction, the grid is clustered from y^+=60 at the upper edge to y^+=1 at the wall and the maximum grid stretching factor is no more than 1.15. Besides, in the downstream location from x=20δ to x=24δ, the grids are stretched to damp the turbulent fluctuations and prevent their reflections from the exit boundary. Periodic boundary conditions are applied in the spanwise direction for all variables, and no-slip boundary condition is imposed upon the adiabatic wall. The wall condition for specific dissipation rate ω employs Menter's automatic omega wall function. At the inflow boundary, a sponge layer is applied to the energy equation to damp unphysical pressure fluctuations generated by the synthetic turbulence generation methods. The sponge layer thickness is assumed 2δ and the sponge layer coefficient is linearly decreasing in the streamwise direction from the inflow boundary to the edge of the sponge layer. The damping is only applied to the energy equation and not explicitly to the continuity and momentum equations. This formulation ensures that the shape of the synthetic eddies is not significantly modified. Further details of the sponge layer formulation are given in Zhang[42]. The time-step size in this case is set to Δt=3e-8s, which corresponds to a nondimensional time-step of $\Delta t^{+}=\Delta t u_{\tau}^{2}/\nu=0.1$ in wall units. In the following, the statistics are averaged at the location of x=6δ in time and in the spanwise direction.

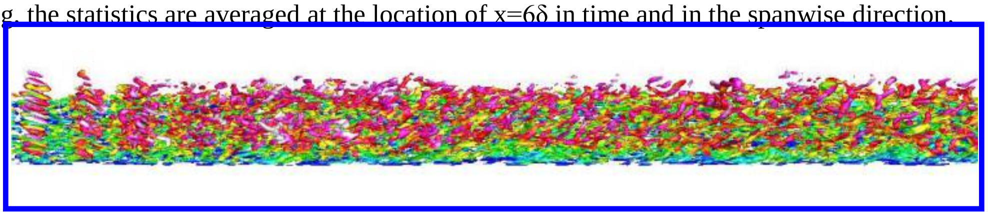

Figure 11. Coherent turbulent structures based on Q-criterion with mapped-on local Mach number

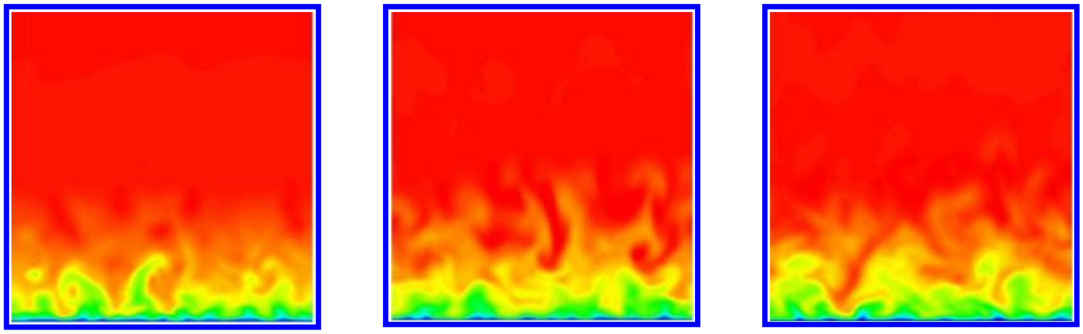

a) **x=2δ** **b)** **x=4δ** **c)** **x=6δ**

Figure 12. Instantaneous streamwise velocity field at three crossflow planes

A snap of the turbulent flowfield is visualized in Fig.11. This image displays the coherent turbulent structures based on the Q-criterion colored by Mach number. Near the inflow boundary of the LES domain at x<δ elongated structures are already clearly visible, which are the initial vortices introduced by synthetic turbulence method. In the downstream, these eddies gradually break down: ejected vortices are observed on the outer edge and elongated structures evolve in the streamwise direction near the wall surface, which resembles the typical turbulent structures of a wall-bounded turbulence solution. These vortices emphasize the progressive increase of turbulent production in this region. Similar facts are also illustrated in Fig.12, where the contours of streamwise velocity at three crossflow planes are displayed. These results show that the fully developed wall-bounded turbulence is quick to establish in a short transition distance with the higher degree of realism of the inflow data provided by the synthetic turbulence method. What's more, the excellent capability of the low-dissipation solver hybridCentralFoam in resolving the wall-bounded turbulence is well validated.

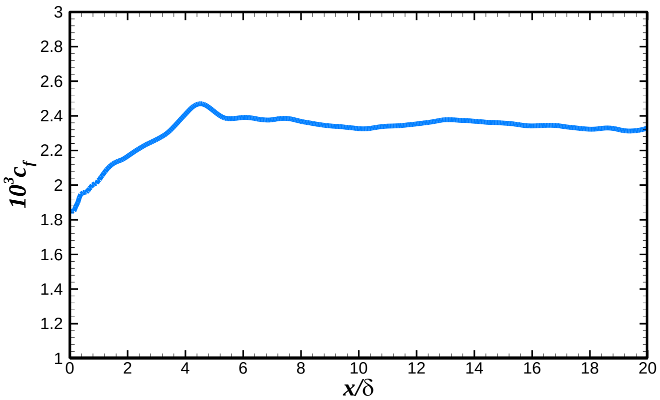

Figure 13. Streamwise development of the spanwise averaged skin-friction coefficient

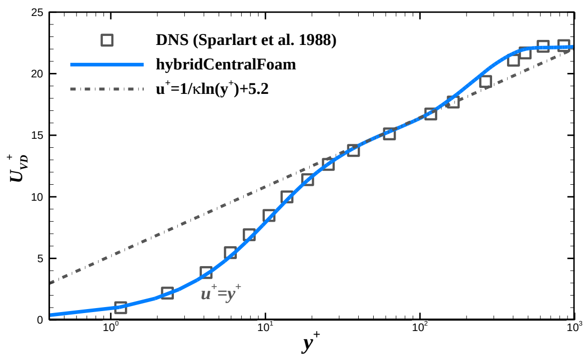

Figure 14. Spanwise averaged mean velocity profile at location x=6δ

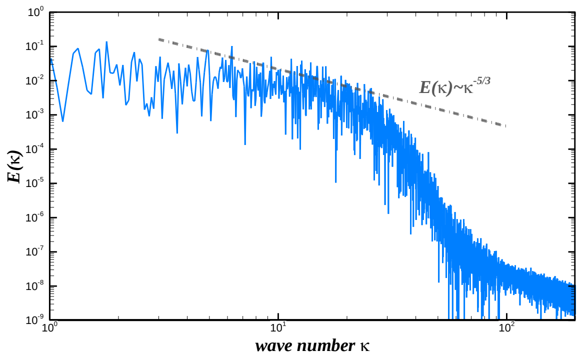

Figure 15. Power spectral of the turbulent kinetic energy at location x=6δ and y^+=200

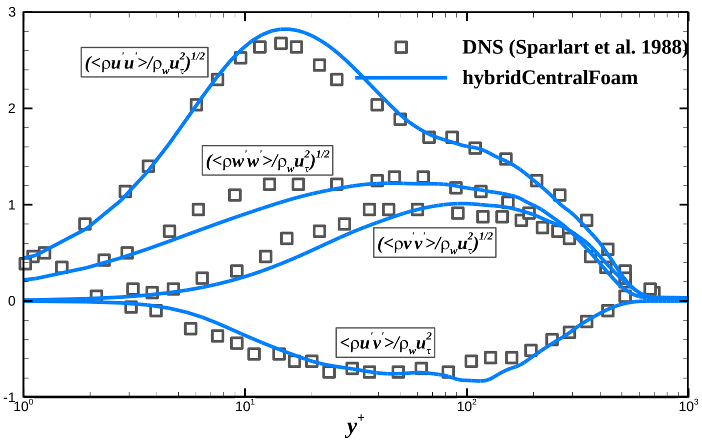

Figure 16. Normalized streamwise, spanwise, and wall-normal root of the mean squared velocity fluctuations and Reynolds shear stress profiles at location x=6δ

The streamwise development of the skin-friction coefficient c_f is presented in Fig.13. In the downstream of inflow boundary, the c_f value drops slightly in the initial stage and then converges to correct c_f-level within approximately five or six boundary-layer thicknesses (5-6δ). That means that the turbulent structures generated by synthetic turbulence method possess a proper shape and a physical spectral content in the inner of the boundary layer such that the transition length to recover is short. The time and spanwise averaged velocity profile at x=6δ is shown in Fig.14. The van Driest transformed velocity profile solved by low-dissipation solver exhibits a satisfying agreement with the DNS data and the log law. Then the fully developed turbulence generated by the inflow method is analyzed through its spectral content. The power spectral of turbulent kinetic energy at a nondimensional wall-normal position y^+=200 is plotted in Fig.15. The turbulent kinetic energy signal has a continuous distribution from low wave number to high wave number, though the low-frequency content still dominates it. Meanwhile, the power spectral of the turbulent kinetic energy follows the Kolmogorov's -5/3 law. All this indicate that suitable turbulence structures that contains correct energy spectrum have established and the compressible wall-bounded turbulent flow have recovered to the fully developed state at x=6δ. Fig.16 illustrates the streamwise, spanwise and wall-normal root of the mean squared velocity fluctuations and Reynolds shear stress profiles at x=6δ, which are normalized by the wall shear stress. One can notice that all the velocity fluctuations as well the Reynolds shear stress obtained by synthetic turbulence method succeed in reproducing the statistics distribution by the DNS solution to an incompressible flow at a momentum number Re_θ=2000. Close observations will find out that the streamwise velocity fluctuation in the inner boundary layer is slightly overestimated, whereas the spanwise and wall-normal fluctuations are mildly underestimated. This is due to the unavoidable numerical dissipation caused by insufficient grid resolution near the wall surface.

V. Application to Realistic Flow

In order to examine the low-dissipation solver's performance in the flame holder structure in the scramjet model, a supersonic flow over a rearward facing step and subsequent reattachment along an inclined wall is investigated with the IDDES method based on Menter's k-ω SST model in conjunction with turbulence inflow conditions. This configure contains massive flow separation as well as shock/turbulent boundary layer interactions, which are common in hypersonic propulsion flowpaths. The simulation results will be compared with the experimental measurements, including the velocity profiles along the shear layer and above the ramp wall, in order to validate the low-dissipation solver's performance in such a complex flow.

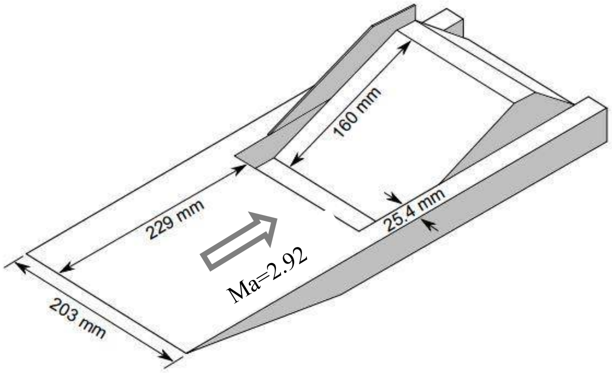

Figure 17. Geometry sketch of the experimental model with one aerodynamic fence removed

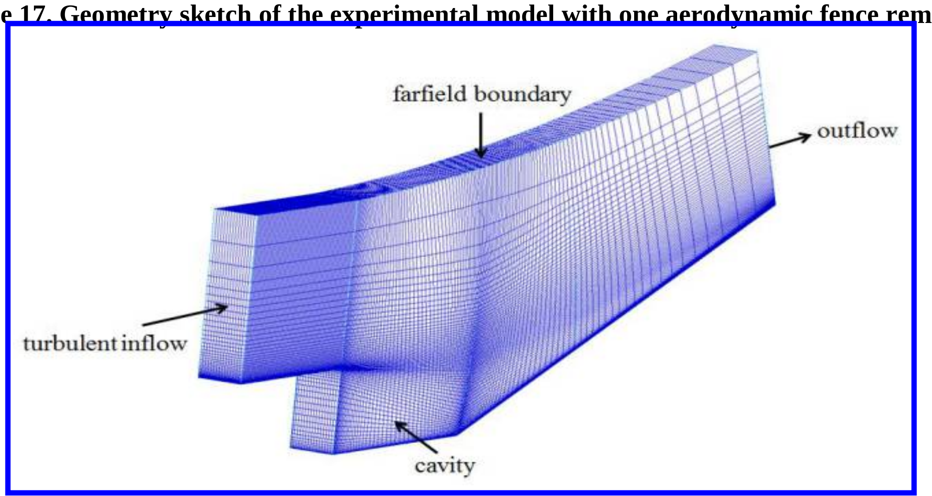

Figure 18. Isometric view of the computational domain with coarsened grids for visual clarify

The flow chosen for the current investigation were extensively studied by Baca[43] and Settles[44] in the Princeton University 8 inch by 8 inch high Reynolds number, blow down, supersonic wind tunnel. Nominal conditions for the experiment were at a stagnation pressure of p_0 =0.69Mpa ±1%, a stagnation temperature of T_0 =258K ±4%, a freestream Mach number of Ma_∞=2.92 ±0.015, and a free stream unit Reynolds number of 6.7×10^7/m ±4%. Fig.17 illustrates the basic geometry involved for the experiment. The test model was constructed from brass, and consisted of a wedge-shaped plate with a cavity, 25.4 mm deep and 61.9 mm long, followed by a 160 mm long 20° ramp. The cavity and ramp were only 152.4 mm wide, with a 25.4 mm inset between them and the tunnel walls on both sides to prevent effects from the tunnel wall boundary layers. The cavity depth was 25.4mm, and the model was sized and central in the test section to ensure that it was not directly influenced by the tunnel sidewall boundary layers. In order to promote two-dimensionality of the experiment, aerodynamic fences were attached to the portion of the ramp, which extended above the cavity to help ensure two-dimensionality of the flowfield. A traversing set of Pitot and static pressure probes were used to conduct the experimental measurements. The mean flow properties were extracted in conjunction with the assumption of constant total temperature. Specially, several boundary layer profiles at 25.4mm upstream of the cavity were measured in the experiments to obtain the local boundary layer properties.

Simulations are performed on a three dimensional grid, which consists of approximately 16 million cells, which is briefly illustrated in Fig.18. The streamwise, spanwise, and wall-normal dimensions of the blocks directly upstream and downstream of the backward-facing step is 255×155×134 and 301×155×234, respectively. The physical dimensions in the streamwise, spanwise, and wall-normal directions of the computational domain are 26.2cm, 1.3cm, and 5.0cm. The flat plate extended two step heights upstream to allow sufficient distance for the inflow turbulence developing into fully developed state, where the grid are clustered in the streamwise direction to meet the requirement of synthetic turbulence method. Downstream of the backward-facing step, a more isotropic grid is generated for the free shear layer. The grid is clustered to provide a nominal $y^+ \approx 1.0$ adjacent to the surface. The physical time step is set to 0.01μs with the maximum CFL number of 0.9. The flowfield is initialized with a converged flowfield simulated by a RANS simulation on a courser grid set. Statistics are taken after the flowfield evolves for a minimum of three characteristic flow-through times. Once a stationary state is achieved, the flowfield begin ensemble averaged and subsequently spatially averaged in the homogeneous spanwise direction.

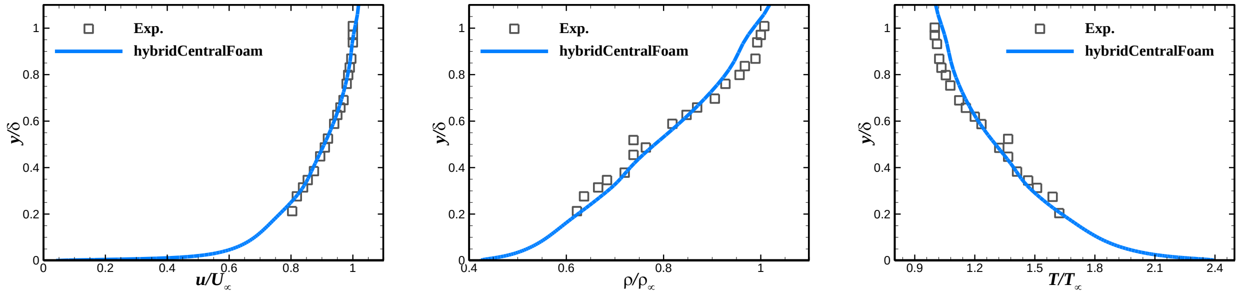

a) Velocity profile **b) Density profile** **c) Temperature profile**

Figure 19. Comparison of experimentally measured and extracted boundary layer profiles at 25.4mm upstream of cavity

In the current simulation, all walls are assumed with adiabatic and no-slip boundary conditions and periodic boundary conditions are applied in the spanwise direction. In addition, supersonic inflow and outflow conditions are imposed on the inlet and outlet boundary, and a characteristic condition is applied at the farfield boundary with the stretched grids using to damp the fluctuations and prevent the wave reflection. In order to introduce coherent turbulent structure at the inflow boundary, synthetic turbulence method is employed for the velocity and temperature profiles. As a preliminary verification of such method, Fig.19 shows the comparisons of the time-averaged velocity, density, and temperature profiles between the experimental data and the extracted boundary layer from current simulation at 25.4mm upstream of the cavity. The results demonstrate that synthetic turbulence method could generate nearly realistic mean flow condition at the upstream of the cavity. In addition, the turbulent inflow will also provide rich turbulent fluctuations and coherent turbulent structures to the downstream, which are mostly resolved by the current grid setting and IDDES method. This will help make a better simulation of the complex flowfield in the downstream.

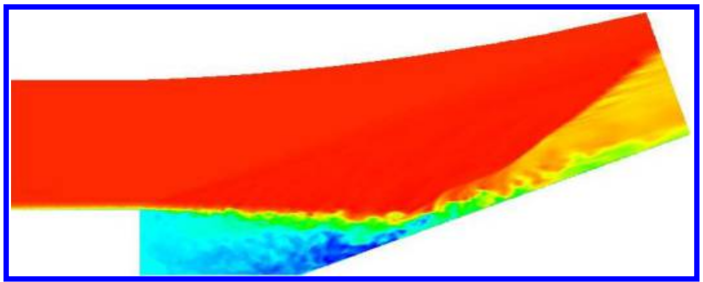

Figure 20. Snapshot of instantaneous streamwise velocity field

Figure 21. Snapshot of instantaneous density gradient magnitude

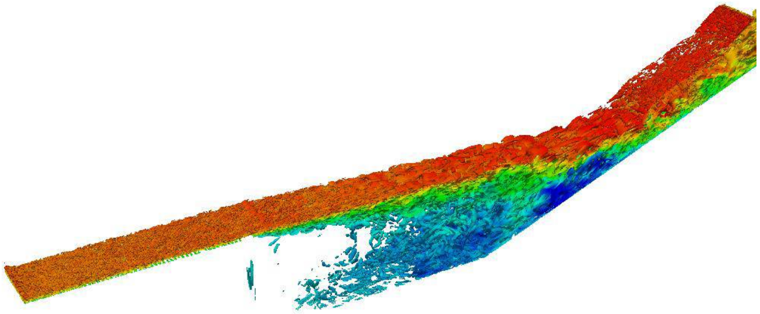

Figure 22. Turbulent structures visualized via the Q-criterion with mapped-on streamwise velocity

A snapshot of the instantaneous streamwise velocity contours is highlighted in Fig.20. The major flow features observed in the experiment are well reproduced in the simulation. The turbulent inflow evolves along the flat plate, and then detach at the corner of the step, creating a free shear layer over the cavity. When it reattaches along the ramp, the free shear layer will interact with an oblique shock front standing off the ramp, and the flow will be entrained into the cavity near this reattachment location. Thereby, a recirculation zone comes into being, which will drive an unsteady low-frequency motion of the shear layer. Besides, a slight expansion fan forms off the corner of the step, but it is not observed in the experiment due to the constant pressure conditions setting under the free shear layer. The periodic boundary condition in the spanwise direction is responsible for such phenomenon. By taking the gradient magnitude of the instantaneous density field, as shown in Fig.21, a pseudo numerical schlieren is created, which makes the shear layer, turbulent structures, and shock system easier to identify. Fig.22 presents the contour image of the turbulent structure visualized via iso-surfaces of Q-criterion with mapped-on streamwise velocity. The results demonstrate that fine-scale wall-bounded turbulent structures slowly evolve along the flat plate in the upstream. As the flow separates from the corner of the backward-facing step, much larger structures come into being, which corresponds to the free shear layer and recirculation zone. It's also evident that the recompression shock after reattachment has a pronounced effect on the turbulence structure.

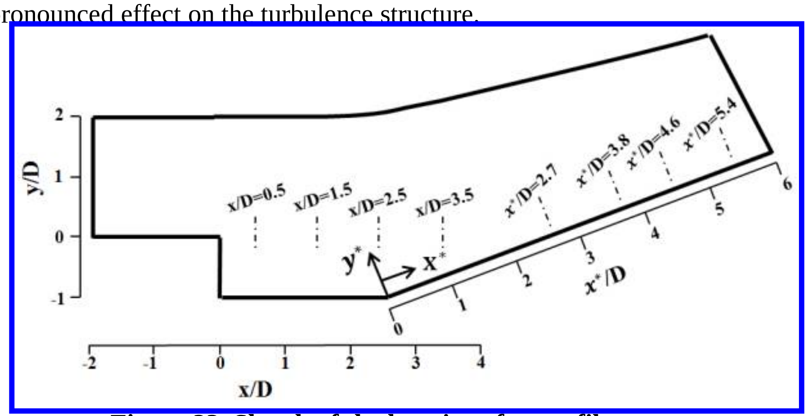

Figure 23. Sketch of the locations for profile surveys

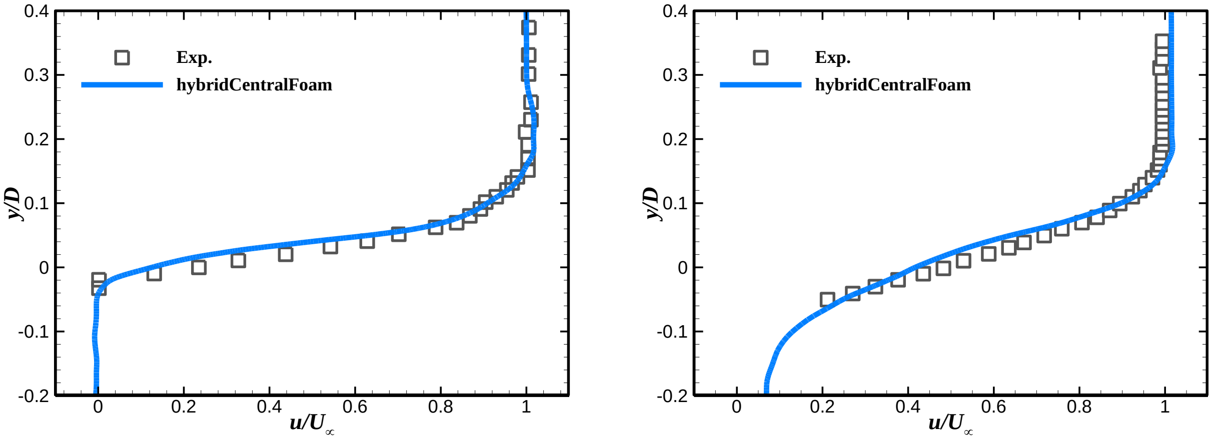

a) x=0.5D **b) x=1.5D**

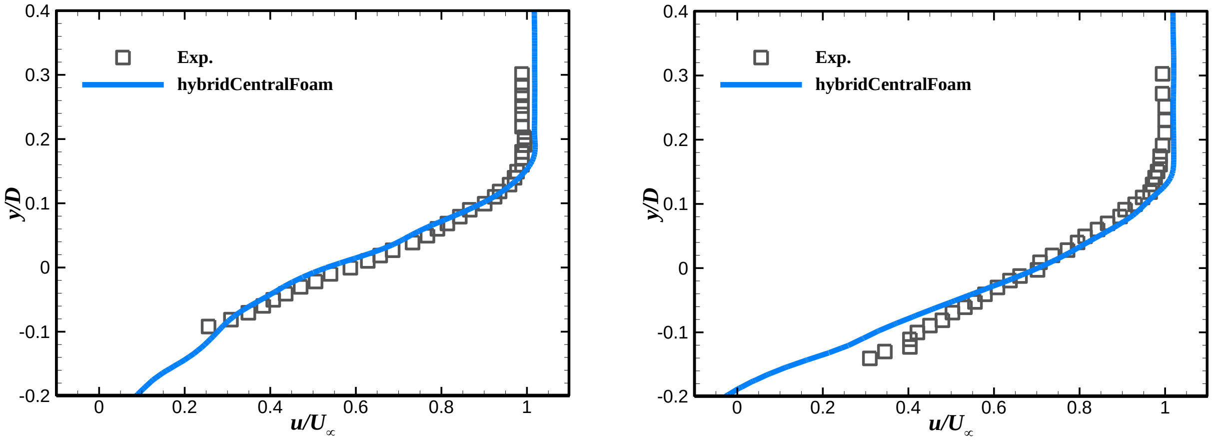

c) x=2.5D d) x=3.5D

Figure 24. Normalized velocity profiles through the shear layer

As previously mentioned, several measured profile surveys of the shear layer above the cavity and the boundary layer along the ramp are available from the experiments. For ease of reference, the locations of these profiles are shown in Fig.23. Here the streamwise and normal directions have been normalized by the step height of D=25.4 mm. Comparisons of the time-averaged flow properties for normalized velocity profiles through the shear layer with the available experimental data are illustrated in Fig.24. In the simulation, the flowfield actually is treated as a quasi-two-dimensional problem, since the cyclic boundary conditions are applied in the spanwise direction. However, such treatment will lead to the flow not to be totally reproduced. In this case, the low pressure in the cavity, the downward deflection of the free shear layer as well as the slight expansion above the cavity all are directly related to insufficient consideration of the three-dimensionality features of this flowfield. In order to concentrate our focus on the spreading rate of the shear layer, the free shear layer is shifted by a small rotation angle to line up the bulk location of the shear layer with the experimental data. Once the shear layer is shifted, the velocity profiles through it agree quite well with the measured spreading rate as depicted in Fig.24.

Predictions of the normalized static pressure along the ramp wall and velocity profiles across the ramp boundary layer are shown in Fig.25 and Fig.26, respectively. The results of the simulation are not in good agreement with the experimental measurements. This is not surprising. Compared to the experiments, the flowfield will endure lower pressure at the bottom of the ramp due to slight expansion of the upstream shear layer, and then experience earlier pressure rising as the downward deflection of the shear layer collides with the ramp. Similar logics can also be used to explain the velocity profiles mismatch in the inner boundary layer of the reattachment ramp illustrated in Fig.26. As the free shear layer deflects downward, the downstream flowfield will experience earlier occurrence of flow reattachment. Thereby the inner velocity profiles along the ramp in the downstream will undergo premature boundary layer recovery state, though the velocity profiles in the outer boundary layer agree well with the experimental data.

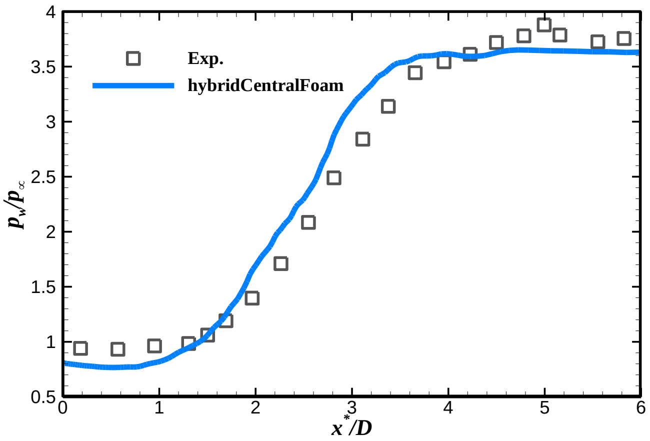

Figure 25. Normalized wall pressure distribution along the reattachment ramp

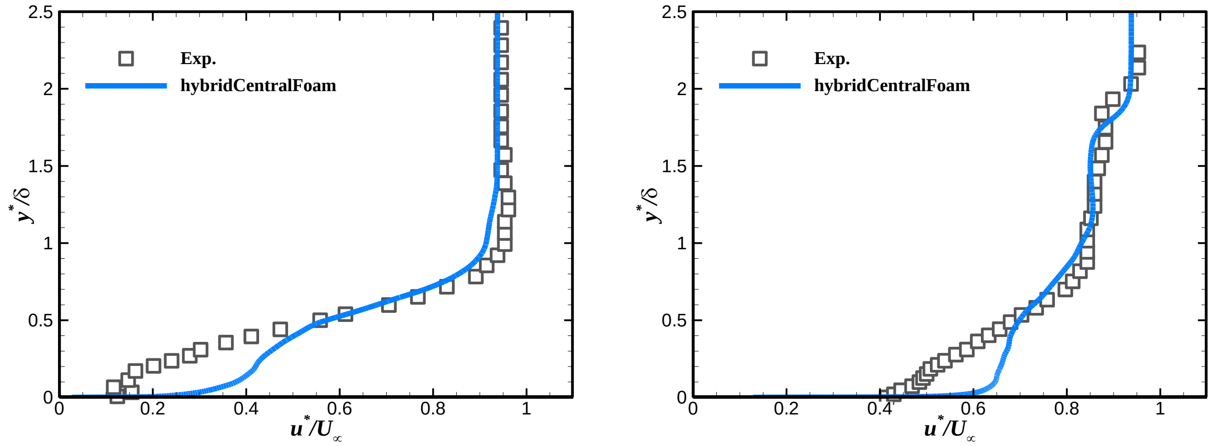

a) x^***=2.7D** **b)** x^***=3.8D**

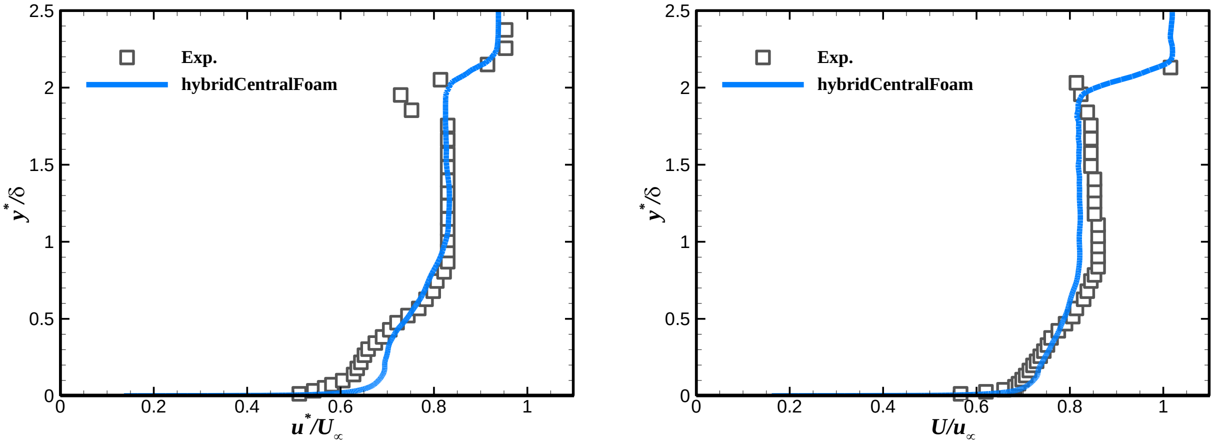

c) x^***=4.6D** **d)** x^***=5.4D**

Figure 26. Normalized velocity profiles normal to the reattachment ramp surface

VI. Conclusion

In this study, a low-dissipation compressible solver for large eddy simulation is developed in the framework of the open source platform OpenFOAM. The new solver combines a dissipative scheme with excellent shock-capturing capability and the central scheme with nondissipative property into a hybridized scheme, in order to deal with the supersonic turbulent flows in the scramjet. The sock sensor plays a key role in the hybridization formulation, and determines the numerical dissipation of the flow modeling to a large degree. Here a modified Ducros sensor is employed to activate the dissipative scheme only in the vicinity of strong shock waves. Furthermore, the third order TVD Runge-Kutta time marching method and a hybrid RANS/LES method based on the k-ω SST model is implemented in the low-dissipation solver to reduce the temporal dissipation and to deal with the wall-bounded flow. Besides, a forth order central scheme have been formulated and to reduce the dispersion error of the low-dissipation solver.

The hybrid scheme based solver has been validated by a series of benchmark problems, including Sod shock tube test, Shu-Osher problem, Green-Taylor vortex evolution and wall-bounded turbulent flow. The performance of the low-dissipation solver in both resolving turbulence and capturing flow discontinuities is verified through the extensive comparisons with the experimental data and DNS results. In addition, synthetic turbulence method using the low-dissipation solver is proved to be an effective method to generate compressible turbulence inflow for LES. The simulation of supersonic flow over a cavity ramp configuration further validated the low-dissipation solver's reliability and robustness in solving the flowfield with complex multiple scales. At the same time, the test case also emphasizes the importance of three-dimensional effect in modeling realistic flows.

Overall, much attention in current research has been paid to the dissipative performance of the new solver, whereas the dispersion property is less emphasized. In addition, the performance of the low-dissipation solver in simulating the internal flow with realistic configurations and supersonic reacting flows are still not fully tested. Further research work should focus on those issues.

Acknowledgments

The Project was supported by National Natural Science Foundation of China (Grant No. 11502270) and Training Program of the Major Research Plan of the National Natural Science Foundation of China (Grant No. 91641110). The authors are also grateful to National Supercomputer Center in Tianjin for providing computational resource.

References

[1] Kurganov, A., Tadmor, E., “New High-Resolution Central Schemes for Nonlinear Conservation Laws and Convection-Dissipation Equations,” Journal of Computational Physics, Vol. 160, No.12, 2000, pp. 241-282.

[2] Lax, P., “Weak solutions of nonlinear hyperbolic equations and their numerical computation,” Communications on pure and applied mathematics, Vol. 7, No. 1, 1954, pp. 159-193.

[3] Nessyahu, H., Tadmor, E., “Non-oscillatory central differencing for hyperbolic conservation laws,” Journal of computational physics, Vol. 87, No. 2, 1990, pp. 408-463.

[4] Colonius, T., Lele, S., “Computational aeroacoustics: Progress on nonlinear problems of sound generation,” Progress in Aerospace Sciences, Vol. 40, No. 6, 2004, pp. 345-416.

[5] Honein, A., Moin, P., “Higher entropy conservation and numerical stability of compressible turbulence simulations,” Journal of computational physics, Vol. 201, No. 2, 2004, pp. 531-545.

[6] Pirozzoli, S., “Numerical Methods for High-Speed Flows,” Annual Review of Fluid Mechanics, Vol.43, August 13, 2010, pp. 163-194.

[7] Adams, N., Shariff, K., “A high-resolution hybrid compact-ENO scheme for shock-turbulence interaction problems,” Journal of computational physics, Vol.127, No. 1, 1996, pp. 27-51.

[8] Pirozzoli, S., “Conservative hybrid compact-WENO schemes for shock-turbulence interaction,” Journal of computational physics, Vol.178, No. 1, 2002, pp. 81-117.

[9] Hill, D., Pantano, C., Pullin, D., “Large-eddy simulation and multiscale modeling of a Richtmyer-Meshkov instability with reshock,” Journal of fluid mechanics, Vol.557, June 2006, pp. 29-61.

[10] Pantano, C., Deiterding, R., Hill, J., Pullin, D., “A low numerical dissipation patch-based adaptive mesh refinement method for large-eddy simulation,” Journal of computational physics, Vol.221, No. 1, 2007, pp.63-87.

[11] Ducros, F., Ferrand, V., Nicoud, F., Wber, C., Darracq, D., Gacherieu, C., Poinsot, T., “Large eddy-simulation of the shock/turbulence interaction,” Journal of computational physics, Vol.152, February 4, 1999, pp.517-549.

[12] Yee, H., Sjogreen, B., “Development of low dissipative high order filter schemes for multiscale Navier-Stokes/MHD systems,” Journal of computational physics, Vol.225, No. 1, 2007, pp.910-934.

[13] Kennedy, C., Gruber, A., “Reduced aliasing formulations of the convective terms within the Navier–Stokes equations for a compressible fluid,” Journal of computational physics, Vol.227, 2008, pp.1676-1700.

[14] Tam, C., Webb, J., “Dispersion-relation-preserving finite difference schemes for computational acoustics,” Journal of computational physics, Vol.107, 1993, pp.262-281.

[15] Lele, S., “Compact finite difference schemes with spectral-like resolution,” Journal of computational physics, Vol. 103, No. 1, 1992, pp.16-42.

[16] Kok, J. C., “a High-Order Low-Dispersion Symmetry-Preserving Finite-Volume Method for compressible flow on curvillinear grids,” Journal of computational physics, Vol. 228, No.4, 2008, pp. 6811-6832.

[17] Peterson, D. M., “Simulations of injection, mixing, and combustion in supersonic flow using a hybrid RANS/LES Approach,” Ph.D. Dissertation, the University of Minnesota, 2011.

[18] Khalighi, Y., Nichols, J. W., Ham, F., Lele, S. K., Moin, P., “Unstructured Large Eddy Simulation for Prediction of Noise Issued from Turbulent Jets in Various Configurations,” AIAA Paper, 2010, 17th AIAA/CEAS Aeroacoustics Conference, Oregon, Portland, Jun 6-8.

[19] Lowe, J., Probst, A., Knopp, T., Kessler, R., “A low- dissipation low-dispersion second-order scheme for unstructured finite-volume flow solvers,” 53rd AIAA aerospace sciences meeting, Kissimmee, Florida, 2015-0815.

[20] Pirozzoli, S., Bernardini, M., Grasso, F., “Direct numerical simulation of transonic shock/boundary layer interaction under conditions of incipient separation,” Journal of fluid mechanics, Vol.657, August 2010, pp. 361–93.

[21] Jameson, A., Schmidt, W., Turkel, E., “Numerical simulation of the Euler equations by finite volume methods using Runge-Kutta time stepping schemes,” AIAA journal 81-1259, July 1981.

[22] Hill, D., Pullin, D., “Hybrid tuned center-difference-WENO method for large-eddy simulations in the presence of strong shocks,” Journal of computational physics, Vol. 194, No.2, 2004, pp. 435-450.

[23] Visbal, M., Gaitonde, D., “Shock capturing using compact-differencing-based methods,” 43rd AIAA Aerospace Sciences Meeting Exhibition, Reno, AIAA Paper, 2005-1265.

[24] Kawai, S., Shankar, S., Lele, S., “Assessment of localized artificial diffusivity scheme for large-eddy simulation of compressible turbulent flow,” Journal of computational physics, Vol. 229, No.5, 2010, pp. 1739-1762.

[25] Bhagatwala, A., Lele, S., “A modified artificial viscosity approach for compressible turbulence simulations,” Journal of computational physics, Vol. 228, April 2009, pp. 4965-4969.

[26] Gottlieb, S., Shu, C., “Total variation diminishing Runge-Kutta schemes,” Mathematics of computation, Vol. 67, No. 221, 1998, pp. 73-85.

[27] Shur, M. L., Spalart, P. R., Strelets, M. K. and Travin, A. K., “A Hybrid RANS-LES Approach with Delayed and Wall-Modelled Capabilities,” International Journal of Heat and Fluid Flow, Vol. 29, No.6, 2008, pp. 1638-1649.

[28] Gritskevich, M. S., Garbaruk, A. V., Schutze, J. and Menter, F. R., “Development of DDES and IDDES Formulations for the k-w Shear Stress Transport Model,” Flow Turbulence Combust, 2011.

[29] Greenshields, C., Weller, H., Gasparini, L., Reese, J., “Implementation of semi-discrete, non-staggered central schemes in a coloated, polyhedral, finite volume framework, for high-speed viscous flows,” International Journal for numerical methods in fluid, Vol. 63, No. 1, 2010, pp.1-21.

[30] Sod, G. A., “A Survey of Several Finite Difference Methods for Systems of Nonlinear Hyperbolic Conservation Laws,” Journal of computational physics, Vol. 27, No.1, 1978, pp. 1-31.

[31] Shu, C., Osher, S., “Efficient Implementation of Essentially Non-Oscillatory Shock-Capturing Schemes,” Journal of computational physics, Vol. 83, No.9, 1989, pp. 32-78.

[32] Augoula, A. B., “A Hybrid Finite Difference-WENO Scheme for Large Eddy Simulation of Compressible Flows,” Proceedings of the European Workshop HONOM 2013, edited by R. Abgrall et al, France, March 18-22, 2013, pp. 15-36.

[33] Emery, S., “An evaluation of several differencing methods for inviscid fluid flow problems,” Journal of computational physics, Vol. 2, No.3, 1968, pp. 306-331.

[34] Woodward, P., Colella, P., “The numerical simulation of two-dimensional fluid flow with strong shocks,” Journal of computational physics, Vol. 54, No.1, 1984, pp. 115-173.

[35] Johnsen, E., Larsson, J., Bhagatwala, A. V., Cabot, W. H., Moin, P., Olson, B. J., Rawar, P. S., Shankar, S. K., Sjogreen, B., Yee, H. C., Zhong, X. and Lele, S. K., “Assessment of High-resolution Methods for Numerical Simulations of Compressible Turbulence With Shock Waves,” Journal of computational physics, Vol. 229, No. 4, 2010, pp. 1213–1237.

[36] Brachet, M. E., Meiron, D. I., Orszag, S. A., Nickel, B. G., Morf, R. H., and Frisch, U., “Small-scale structure of the Taylor-Green vortex," Journal of fluid mechanics, Vol. 130, 1983, pp. 411 -452.

[37] van Rees, W. M., Leonard, A., Pullin, D., and Koumoutsakos, P., “A comparison of vortex and pseudo-spectral methods for the simulation of periodic vortical flows at high Reynolds numbers," Journal of computational physics, Vol. 230, No. 8, 2011, pp. 2794-2805.

[38] Roidl, B., Meinke, M., and Schroder, W., “A Reformulated Synthetic Turbulence Generation Method for a Zonal RANS-LES Method and its Application to Zero-Pressure Gradient Boundary Layers,” International Journal of Heat and Fluid Flow, Vol. 44, No.3, 2013, pp. 28-40.

[39] Jarrin, N., Benhamadouche, S., Laurence, D., Prosser, R., “A synthetic-eddy-method for generating inflow conditions for large-eddy simulations,” International Journal of Heat and Fluid Flow, Vol. 27, No.4, 2006, pp. 585-593.

[40] Pamies, M., Weiss, P., Garnier, E., Deck, S., Sagaut, P., “Generation of synthetic turbulent inflow data for large eddy simulation of spatially evolving wall-bounded flows,” Physics of fluids, Vol. 21, No. 4, 2009(045103).

[41] Spalart, P. R., “Direct simulation of a turbulent boundary layer up to Re_θ=1410,” Journal of Fluid Mechanics, Vol.187, February 1988, pp. 61-98.

[42] Zhang, Q., Schroder, W., Meimke, M., “A zonal RANS-LES method to determine the flow over a high-lift configuration,” Computers & Fluids, Vol. 39, No. 7, 2010, pp.1241-1253.

[43] Beca, B. K., “An Experimental study of the reattachment of a free shear layer in compressible turbulent flow,” Master’s thesis, Princeton University, Princeton, NJ, 1981.

[44] Settles, G. S., Williams, D. R., Baca, B. K. and Bogdonoff, S. M., “Reattachment of a Compressible Turbulent Free Shear Layer,” AIAA Journal, Vol. 20, No.1, 1982, pp. 60-68.

This article has been cited by:

1. Pankaj Rajput, Sunil Kumar. Directionally Targeted Jet Noise Suppression: Benefits of Asymmetric Downstream Fluidic Injection . [Citation] [PDF] [PDF Plus]